Appl. Phys. A 81, 1363–1368 (2005)
DOI: 10.1007/s00339-005-3264-7

Applied Physics A
Materials Science & Processing

Thin porous indium tin oxide nanoparticle films: effects of annealing in vacuum and air

J. EDERTH[1]
A. HULTÅKER[1,✉]
G.A. NIKLASSON[1]
P. HESZLER[1,2]
A.R. VAN DOORN[3]
M.J. JONGERIUS[3]
D. BURGARD[4]
C.G. GRANQVIST[1]

[1] Department of Engineering Sciences, The Ångström Laboratory, Uppsala University, PO Box 534, 75121 Uppsala, Sweden
[2] Research Group of Laser Physics of the Hungarian Academy of Sciences, University of Szeged, Box 406, 6701 Szeged, Hungary
[3] Philips Applied Technologies, PO Box 218/SAQ, 5600 MD Eindhoven, The Netherlands
[4] Nanogate GmbH, Gewerbepark Eschberger Weg, 66121 Saarbrücken, Germany

Received: 7 February 2005/Accepted: 16 March 2005

ABSTRACT Electrical and optical properties were investigated in porous thin films consisting of In_2O_3:Sn (indium tin oxide; ITO) nanoparticles. The temperature-dependent resistivity was successfully described by a fluctuation-induced tunneling model, indicating a sample morphology dominated by clusters of ITO nanoparticles separated by insulating barriers. An effective-medium model, including the effect of ionized impurity scattering, was successfully fitted to measured reflectance and transmittance. Post-deposition treatments were carried out at 773 K for 2 h in both air and vacuum. It is shown that vacuum annealing increases either the barrier width or the area between two conducting clusters in the samples and, furthermore, an extra optical absorption occurs close to the band gap. A subsequent air annealing then reduces the effect of the barriers on the electrical properties and diminishes the absorption close to the band gap.

PACS 72.80.Jc; 81.07.Bc; 81.40.Tv

1 Introduction

Indium tin oxide (ITO) is a material capable of showing low optical absorption for visible light together with good electrical conductivity. Materials with these properties are of importance in a number of different applications, and they can be used as transparent electrodes in optical switching and display devices as well as in solar cells, to name a few [1].

Thin films of ITO are most often produced by physical vapor deposition [2–4] or by spray pyrolysis [5]. High-quality ITO films have a transmittance of approximately 90% in the visible-wavelength range, and the electrical resistivity can be as low as 1 to $4 \times 10^{-4}\ \Omega$ cm [6].

Physical vapor deposition is a time-consuming and expensive deposition method. Furthermore, in many applications, for example for display devices, a patterned front-electrode structure is required, which introduces several extra process steps in the production route, including etching. It is of significant interest to reduce the number of process steps, thereby yielding faster production and lower cost. This can be realized by a screen-printing process, wherein a dispersion of ITO nanoparticles is printed directly on to the substrate, followed by heat treatment in order to produce high electrical conductivity in the patterned ITO structure. However, there are several problems that have to be overcome to achieve a device with adequate performance, i.e. sufficiently low resistivity and high visible transmittance. Parameters that need to be investigated are the solubility of tin in the particles, the porosity in the ITO nanoparticle layers, and effects of annealing on the characteristic parameters of the ITO nanoparticles.

Earlier work of ours [7] has demonstrated that thin films consisting of ITO nanoparticles can be successfully analyzed in terms of charge-carrier concentration and mobility within the nanoparticles, and filling factor of the films, by use of effective-medium theory applied to experimental data on optical reflectance and transmittance in the $0.3\ \mu m < \lambda < 30\ \mu m$ wavelength range.

In the present paper we report a detailed investigation of the effects of annealing on thin porous films consisting of ITO nanoparticles. The charge-carrier concentration and mobility are obtained by applying effective-medium theory, and we compare effects of annealing in vacuum and in oxidizing atmospheres. Further, dc electrical transport properties are investigated by temperature-dependent resistivity measurements in the $77\ K < \theta < 300\ K$ temperature range. One of our main results is the observation of a negative temperature coefficient of resistivity. This is in agreement with a fluctuation-induced tunneling model and indicates that the samples consist of large clusters, containing sintered ITO nanoparticles, separated by insulating barriers.

Section 2 describes sample preparation and characterization. Section 3 then presents optical and electrical properties, and Sect. 4 provides an analysis of the data. The results are discussed in Sect. 5 and conclusions are drawn in Sect. 6.

2 Sample preparation and characterization

ITO nanoparticles with a tin to indium atomic ratio of 5% were produced by a wet-chemical method. Thin films were prepared by spin coating a dispersion of ITO nanoparticles on to glass substrates. Different thicknesses could easily be obtained by adjusting the spin speed and the spin time. Samples used in this investigation had a thickness of approximately 600 nm, as measured on a Tencor Alpha Step 200 me-

---

✉ Fax: +46-18-471-3270, E-mail: annette.hultaker@angstrom.uu.se

Sample	Treatment at 773 K	a [nm]
A	As-deposited	1.0149
B	2 h in vacuum	1.0148
C	2 h in vacuum + 2 h in air	1.0144
D	2 h in air	1.0147

TABLE 1 Sample treatments and data on lattice parameter a

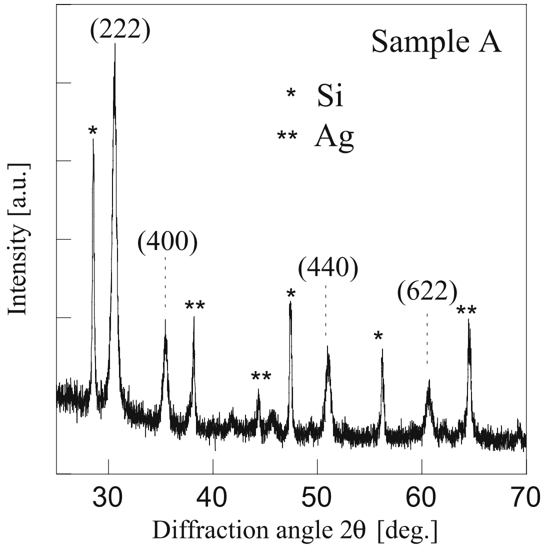

FIGURE 1 X-ray diffractogram of ITO (sample A). The peaks are labeled according to $\mathrm{In_2O_3}$ [9]. Peaks not pertinent to $\mathrm{In_2O_3}$ are labeled according to Si, used as reference material, and Ag, used as contacts for the electrical measurements

chanical stylus instrument. All samples were dried at 393 K for 12 min to remove the dispersion agent from the films. Four different samples were prepared for this investigation by different annealing routes, as given in Table 1. Two different annealing routes are examined: annealing in air and annealing at a pressure of 0.2 mbar (referred to as vacuum).

Crystallinity and grain size d were investigated by X-ray diffractometry (XRD) employing a Siemens D5000 diffractometer operating with Cu K_α radiation at a wavelength of 0.10545 nm. Grain size was evaluated by the Scherrer method [8] using the full width at half maximum of the (222) peak in the appropriate diffractogram. The grain size was found to be ∼ 16 nm; it remained unchanged upon annealing. Figure 1 presents an X-ray diffractogram of sample A. All peaks can be assigned to indium oxide [9], except for peaks pertinent to the Si powder used as reference and Ag from the electrodes.

Lattice-parameter determinations were carried out on all samples. Si powder, put on top of the samples, served as reference material with a well-defined (111) peak; see Fig. 1. The lattice parameter was obtained from the (222) peak for all samples. Data are given in Table 1.

3 Results

3.1 *Optical data*

Normal spectral transmittance T and near-normal spectral reflectance R were measured in the $0.3\,\mu\mathrm{m} < \lambda < 2.5\,\mu\mathrm{m}$ wavelength range using a Perkin Elmer Lambda 9 spectrophotometer equipped with an integrating sphere coated with $\mathrm{BaSO_4}$. Data in Fig. 2a–d show that all samples exhibit a high transmittance, in the range of 90%, within the visible-wavelength range. Samples A and B show a lower transmittance in the near infrared than samples C and D. The reflectance remains low in the whole wavelength range for all samples.

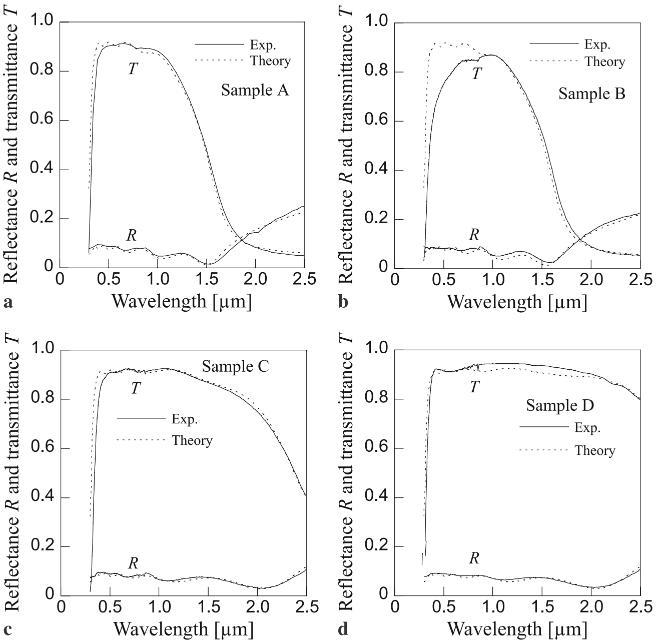

FIGURE 2 Spectral transmittance and reflectance measured for samples A–D, as specified in Table 1, together with theoretical data calculated using the Bruggeman effective-medium theory

Figure 3 presents the absorption coefficient α in the $0.3\,\mu\mathrm{m} < \lambda < 0.8\,\mu\mathrm{m}$ range as obtained from the method of Hong [10]. The films were deposited on to glass substrates, which contribute to the absorption at wavelengths below 400 nm. It is observed that sample B (annealed in vacuum) displays a higher absorption for $\lambda < 1\,\mu\mathrm{m}$ than samples A, C, and D.

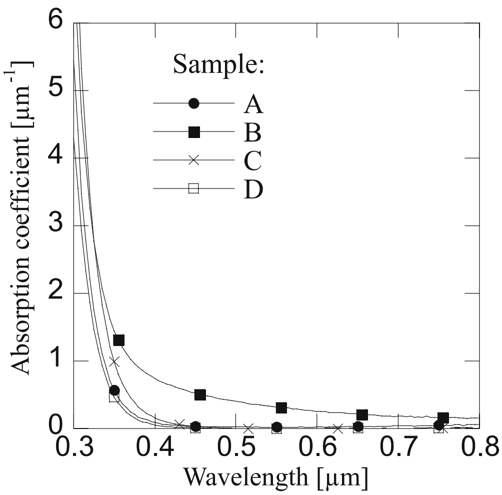

FIGURE 3 Spectral absorption coefficient for samples A–D, as specified in Table 1

Sample	ρ_{RT} [Ω cm]	ρ [Ω cm]	θ_0 [K]	θ_1 [K]
A	0.2	0.0012	149	224
B	0.012	0.0012	240	316
C	0.008	0.0018	155	147
D	0.032	0.0018	172	178

TABLE 2 Data on room-temperature sample resistivity ρ_{RT}, calculated sample resistivity ρ (using (6) and data given in Table 3), and fitting parameters θ_0 and θ_1 used in the fluctuation-induced tunneling model; see (8)

3.2 *Electrical data*

Resistivity ρ was measured for the films using a four-point-probe set-up by recording the voltage when a constant current was passed through the sample. Room-temperature resistivity ρ_{RT} is given in Table 2. The as-deposited sample (sample A) displayed a high electrical resistivity, while annealing in vacuum or/and air reduced the resistivity.

Temperature-dependent resistivity was measured in the $77\,\mathrm{K} < \theta < 300\,\mathrm{K}$ range. Figure 4a–d show data, normalized with the room-temperature resistivity, for all samples. A semiconducting behavior can be noted with a negative temperature coefficient of resistivity (TCR) throughout the whole temperature range.

4 Analysis

4.1 *Optical data*

The ITO particles have diameters that are small enough that the films fulfil the conditions for the quasistatic approximation, i.e. $d \ll \lambda$. Hence the optical data can be analyzed within the framework of an effective medium model theory, specifically using the Bruggeman model [11]. We have earlier published optical data on ITO nanoparticle films and successfully fitted them to an effective-medium model; see [7]. The films were modeled as consisting of spherical ITO nanoparticles with voids of air. The Bruggeman model for effective media comprising such particles reads

$$f\frac{\varepsilon_{\mathrm{p}}-\bar{\varepsilon}^{\mathrm{Br}}}{\varepsilon_{\mathrm{p}}+2\,\bar{\varepsilon}^{\mathrm{Br}}}+(1-f)\frac{\varepsilon_{\mathrm{a}}-\bar{\varepsilon}^{\mathrm{Br}}}{\varepsilon_{\mathrm{a}}+2\,\bar{\varepsilon}^{\mathrm{Br}}}=0, \tag{1}$$

where f is the filling factor of ITO nanoparticles and ε_{p}, ε_{a}, and $\bar{\varepsilon}^{\mathrm{Br}}$ are the dielectric functions for the ITO nanoparticles, air, and for the effective medium, respectively. The Drude model is introduced to represent the frequency (ω)-dependent free-electron properties of the heavily doped degenerate ITO nanoparticles. The Drude model is given by

$$\varepsilon_{\mathrm{p}}=\varepsilon_{\infty}-\frac{\omega_{\mathrm{pl}}^2}{\omega\left(\omega+\mathrm{i}\frac{1}{\tau_0}\right)}, \tag{2}$$

with ω_{pl} and τ_0 according to

$$\omega_{\mathrm{pl}}^2=\frac{n_{\mathrm{e}}e^2}{m_{\mathrm{e}}\varepsilon_0}, \tag{3}$$

$$\tau_0=\frac{m_{\mathrm{e}}}{\rho_{\mathrm{p}}n_{\mathrm{e}}e^2}. \tag{4}$$

Here n_{e} is the charge-carrier concentration, ε_{∞} the optical dielectric constant, ω_{pl} the plasma frequency, τ_0 the free-electron relaxation time, m_{e} the effective electron mass, e the elementary charge, ε_0 the permittivity of free space, and ρ_{p} the resistivity of the ITO nanoparticles.

Hamberg and Granqvist [12] have shown that ionized impurities, introduced in the material through doping, normally provide a dominant source of scattering for the conduction electrons. At frequencies below the screened plasma frequency $\omega_{\mathrm{pl}}/\sqrt{\varepsilon_{\infty}}$, the scattering is approximately energy independent and can be characterized by a constant relaxation time. However, at frequencies above $\omega_{\mathrm{pl}}/\sqrt{\varepsilon_{\infty}}$, the relaxation time is strongly frequency dependent [12]. The effect of ionized impurity scattering (IIS) is implemented in our model by a frequency-dependent relaxation time given by [12, 13]

$$\tau^{\mathrm{IIS}}(\omega)=\tau_0\left(\frac{\omega_{\mathrm{pl}}}{\sqrt{\varepsilon_{\infty}}}\right)^{-3/2}\omega^{3/2}. \tag{5}$$

We use $\varepsilon_{\infty}=4$ in the calculations [14] and set $m_{\mathrm{e}}=0.4\,\mathrm{m}$, where m is the free-electron mass [12]. The expression for τ^{IIS} is put into (2) to replace τ_0 whenever $\omega > \omega_{\mathrm{pl}}/\sqrt{\varepsilon_{\infty}}$. The filling factor in the Bruggeman model is related to the sample resistivity in the dc limit as [15]

$$\rho=\rho_{\mathrm{p}}\left(\frac{1-f_{\mathrm{c}}}{f-f_c}\right), \tag{6}$$

where ρ is the resistivity for the composite and f_{c} is the filling factor corresponding to the percolation limit, which is 0.33 in the Bruggeman model. Thus (6) makes it possible to relate the measured dc resistivity to the resistivity obtained by fitting the Bruggeman model to the experimental data.

Three free parameters were used in adjusting the Bruggeman effective-medium model to the measured reflectance and transmittance, viz. f, n_{e}, and ρ_{p}. From the fitting parameters n_{e} and ρ_{p}, the relaxation time is given by (4). The mobility is obtained from

$$\mu=\frac{e\tau_0}{m_{\mathrm{e}}}. \tag{7}$$

The reflectance and transmittance were calculated for the samples, with proper account taken of the glass substrate. The thin porous ITO film was treated as a single layer [16], using the dielectric function for the composite film derived from the effective-medium theory. The glass substrate was treated in the non-coherent approximation, i.e. only considering light intensities, which were summed to a total reflectance and transmittance. Unpublished optical constants for Corning 7059 glass were used.

Figure 2a–d present experimental spectral data on transmittance and reflectance and fitted data obtained from the effective-medium theory using the Bruggeman model and accounting for ionized impurity scattering. Experiment and theory agree very well for samples A, C, and D. In the case of sample B, there exists a discrepancy at wavelengths close to the band gap. This effect will be discussed in greater detail in Sect. 5. Specific fitting parameters are given in Table 3.

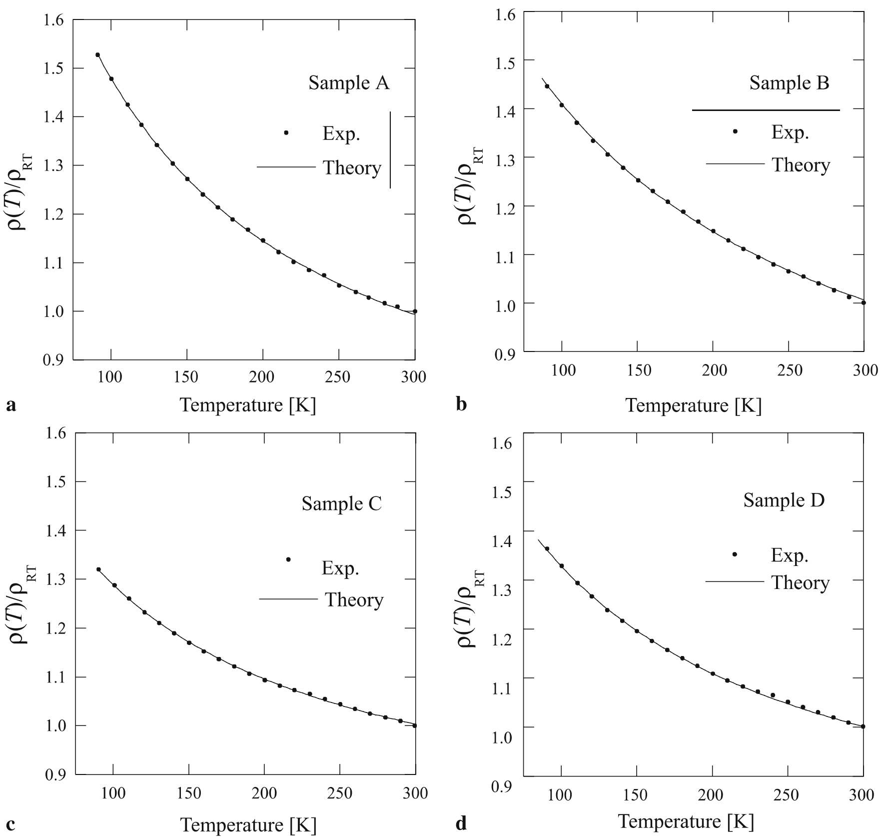

FIGURE 4 *Dots* denote temperature-dependent resistivity $\rho(\theta)$ normalized by the value at room temperature ρ_{RT} for samples A–D, as specified in Table 1. *Solid curves* represent data calculated from the fluctuation-induced tunneling model, using parameters in Table 2

4.2 *Electrical data*

In a recent paper [17] we showed that fluctuation-induced tunneling, i.e. charge transfer between conducting clusters each consisting of many sintered ITO nanoparticles, dominates the temperature-dependent resistivity of porous ITO films. The conducting clusters are large (of the order of μm) and have a high total capacitance, which makes the charging energy negligible compared to the thermal energy. This could be contrasted with the case of a granular metal, where the charging energy dominates the electron transfer between adjacent particles [18, 19]. In our samples the temperature dependence of the resistivity is given by [20]

$$\rho\,(\theta) = \rho_0 \exp\left(\frac{\theta_1}{\theta+\theta_0}\right), \tag{8}$$

where ρ_0, θ_0, and θ_1 are constants, being related to the properties of the insulating barriers between the conducting clusters and given by [21]

$$\theta_0 = \frac{16\varepsilon_0 \hbar A V_0^{3/2}}{\pi\,(2m)^{1/2}\, w^2 e^2 k_{\mathrm{B}}}, \tag{9}$$

$$\theta_1 = \frac{8\varepsilon_0 A V_0^2}{e^2 k_{\mathrm{B}} w}. \tag{10}$$

Here h is Planck's constant divided by 2π, A is the barrier area, V_0 is the barrier height, k_{B} is Boltzmann's constant, and w is the width of the barrier. Figure 4a–d present experimental data adjusted to the fluctuation-induced tunneling model. Table 2 reports the corresponding values for θ_0 and θ_1.

Sample	f	n_{e} [cm^{-3}]	ρ_{p} [Ω cm]	μ [cm^2/V s]
A	0.55	6.2×10^{20}	4×10^{-4}	25
B	0.55	6.0×10^{20}	4×10^{-4}	26
C	0.55	2.7×10^{20}	6×10^{-4}	38
D	0.55	1.8×10^{20}	6×10^{-4}	58

TABLE 3 Fitting parameters, i.e. filling factor f, charge-carrier concentration n_{e}, and resistivity ρ_{p}, together with mobility μ as calculated by (7)

Table 2 shows that θ_0 and θ_1 are strongly increased upon annealing in vacuum (sample B), whereas a following annealing in air decreases both θ_0 and θ_1 (sample C). Annealing in air only (sample D) does not give as low magnitudes of θ_0 and θ_1 as in sample C.

5 Discussion

Figure 2a–d clearly show that the agreement between the experimental data and the effective-medium model, including the effect of ionized impurity scattering, is very good in the whole wavelength range. This gives a strong indication that the transport mechanism within the ITO nanoparticles is dominated by ionized impurity scattering. The filling factor is similar for all samples. Samples A (as-deposited) and B (vacuum annealed) show almost identical n_{e} and μ. However, sample B displays an extra absorption close to the band gap; see Fig. 3. The subsequent annealing in air – yielding sample C – produces a lower n_{e} and a higher μ than those found in samples A and B. The increased mobility is probably due to fewer ionized impurities, i.e. a small number of oxygen vacancies distorting the lattice potential. Annealing in air without the preceding annealing in vacuum (sample D) gives an even lower n_e than in sample C, but the mobility is higher than in this sample; see Table 3.

The dc resistivity of the films can be calculated from (6) using the parameters f and ρ_p, given in Table 3, obtained from fitting the Bruggeman effective-medium model to measured reflectance and transmittance. It is obvious that the calculated sample resistivity ρ is much lower than the measured value ρ_{RT}; see Table 2. The disagreement is largest for sample A, for which the difference is of the order of several magnitudes. This disagreement between calculated and measured dc resistivities indicates that insulating barriers are present between adjacent clusters of particles; such barriers are not included in the modeling of the optical properties of the sample.

The temperature-dependent resistivity is in good agreement with the fluctuation-induced-tunneling model, which indicates a sample morphology with large clusters of ITO nanoparticles; these clusters are separated by insulating barriers.

The parameters θ_0 and θ_1 are related to the barrier height, width, and area; see (9) and (10). Annealing in vacuum significantly increases the parameters θ_0 and θ_1; see Table 2. The amount of increase in θ_0 and θ_1 is of the same order, a factor of 1.6 to 1.8, indicating that the main change is an increased barrier area; see (9) and (10). This notion is supported by the fact that ρ_{RT} is decreased after annealing in vacuum, which means that the number of conducting paths – or the internal area of the existing conduction paths – must have increased. However, it is likely that also the barrier width is slightly decreased since the large decrease in ρ_{RT} cannot only be assigned to an increased barrier area by 1.6 to 1.8. The tunneling probability is exponentially dependent on the barrier width, which means that the sample resistivity is very sensitive to changes in this width.

The following annealing in air – to obtain sample C – gives decreased θ_0 and θ_1 together with a decreased ρ_{RT}. Annealing in air without the preceding vacuum annealing, i.e. sample D, gives a higher ρ_{RT} than in sample C, and θ_0 and θ_1 are also slightly larger. Thus, annealing in vacuum before a final annealing in air gives better film properties – i.e. lower electrical resistivity – than in films annealed in air only.

We have, however, not fully established the structural changes occurring in the samples during the vacuum annealing, and we can only speculate at this stage. The vacuum annealing may increase the oxygen vacancies in the lattice, thereby creating InO_x oxides with x being less than 1.5. It has been shown by Al-Ajili and Bayliss [22] that substoichiometric InO_x exhibits a considerable absorption in the visible region; this absorption was found to increase with decreasing wavelength. We observe a similar behavior in those of our samples that have been annealed in vacuum, thus giving an indication of an increased amount of InO_x with $x < 1.5$. Al-Ajili and Bayliss also showed that the resistivity increased monotonically as x decreased from 1.5 to 1.1. This may explain the change of the barrier parameters θ_0 and θ_1, since it is most likely that the oxygen deficiency occurs close to the surface and the boundaries. A subsequent annealing in air is then expected to diminish the amount of oxygen vacancies, thereby reducing the absorption in the visible range. This is also what we observe in our samples; see Fig. 3. Such a decrease in the concentration of oxygen vacancies would also decrease the effect of the insulating barriers on the resistivity, which is observed for sample C (θ_0 and θ_1 are lower in sample C than in sample B; see Table 2).

From the discussion above, it is apparent that an initial annealing in vacuum, before annealing in air, results in films with higher quality, i.e. lower resistivity, than in films annealed in air only. Annealing in vacuum increases the contact area between adjacent particles and decreases the amount of lattice oxygen in the film. This allows a prolonged annealing time in air, for further sintering of the particles, before oxygen vacancies are removed and Sn ions are deactivated by excess interstitial oxygen leading to the formation of Sn–O complexes.

6 Conclusions

This paper has demonstrated that an initial annealing in vacuum, before annealing in air, improves the electrical properties of films composed of ITO nanoparticles. Films with a room-temperature resistivity of $\sim 8 \times 10^{-3}\ \Omega\,\text{cm}$ were obtained. Samples annealed in air without the preceding vacuum treatment yielded higher resistivity, this typically being $\sim 3.2 \times 10^{-2}\ \Omega\,\text{cm}$. The temperature-dependent resistivity was found to be dominated by tunneling between large clusters of nanoparticles. The electrical transport mechanism within the ITO nanoparticles, on the other hand, is dominated by ionized impurity scattering.

The optical transmittance was seen to be high throughout the visible-wavelength range for most samples, the exception being for samples annealed in vacuum for which an extra absorption close to the band gap could be observed. The optical properties could be reconciled with a theory presuming ionized impurities within the ITO nanoparticles. Thus, the optical properties are given by the properties within the nanoparticles, except for the extra band-gap absorption observed in some samples, and the electrical properties are dominated by the insulating boundaries.

ACKNOWLEDGEMENTS This work was carried out under the auspices of the Center for Advanced Microengineering (AME), financially supported by the Swedish Foundation for Strategic Research, and the European Union through Contract No. BRPR-CT96-0346 (‘Printracon’).

REFERENCES

1 R.G. Gordon: MRS Bull. **25**, 52 (2000)
2 Y. Shigesato, S. Takaki, T. Haranou: Appl. Surf. Sci. **48–49**, 269 (1990)
3 R.B.H. Tahar, T. Ban, Y. Ohya, Y. Takahashi: J. Appl. Phys. **83**, 2631 (1997)
4 N. Kikuchi, E. Kusano, E. Kishio, A. Kinbara, H. Nanto: J. Vac. Sci. Technol. A **19**, 1636 (2001)
5 K. Subba Ramaiah, V. Sundara Raja, A.K. Bhatnagar, R.D. Tomlinson, R.D. Pilkington, A.E. Hill, S.J. Chang, Y.K. Su, F.S. Juang: Semicond. Sci. Technol. **15**, 676 (2000)
6 C.G. Granqvist, A. Hultåker: Thin Solid Films **411**, 1 (2002)
7 J. Ederth, P. Johansson, G.A. Niklasson, A. Hoel, A. Hultåker, P. Heszler, C.-G. Granqvist, A.R. van Doorn, M.J. Jongerius, D. och Burgard: Phys. Rev. B **68**, 155 410 (2003)
8 B.D. Cullity: *Elements of X-ray Diffraction* (Addison-Wesley, Reading, MA 1956)
9 Powder Diffraction File 06-0416, International Centre for Diffraction Data

10 W.Q. Hong: J. Phys. D: Appl. Phys. **22**, 1384 (1989)
11 D.A.G. Bruggeman: Ann. Phys. (Leipz.) **24**, 636 (1935)
12 I. Hamberg, C.G. Granqvist: J. Appl. Phys. **60**, R123 (1986)
13 E. Gerlach, P. Grosse: Festkörperprobleme **17**, 157 (1977)
14 I. Hamberg: Ph.D. Thesis, Chalmers University of Technology, Gothenburg, Sweden (1984)
15 C.G. Granqvist, O. Hunderi: Phys. Rev. B **18**, 1554 (1978)
16 Z. Knittl: *Optics of Thin Films* (Wiley, New York 1976)
17 J. Ederth, P. Heszler, A. Hultåker, G.A. Niklasson, C.-G. Granqvist: Thin Solid Films **445**, 199 (2003)
18 P. Sheng, B. Abeles: Phys. Rev. Lett. **28**, 34 (1972)
19 P. Sheng, B. Abeles, Y. Arie: Phys. Rev. Lett. **31**, 44 (1973)
20 P. Sheng: Phys. Rev. B **21**, 2180 (1980)
21 Z.H. Wang, M.S. Dresselhaus, G. Dresselhaus, K.A. Wang, P.C. Eklund: Phys. Rev. B **49**, 15 890 (1994)
22 A.N.H. Al-Ajili, S.C. Bayliss: Thin Solid Films **305**, 116 (1997)